▌ Nanoparticle Synthesis

Ultrafast Preparation of Monodisperse Fe₃O₄ Nanoparticles by Microwave-Assisted Thermal Decomposition

Yi-Jun Liang,[a] Yu Zhang,*[a, b] Zhirui Guo,[c] Jun Xie,[d] Tingting Bai,[a] Jiemeng Zou,[a] and Ning Gu*[a, b]

Abstract: Thermal decomposition, as the main synthetic procedure for the synthesis of magnetic nanoparticles (NPs), is facing several problems, such as high reaction temperatures and time consumption. An improved a microwave-assisted thermal decomposition procedure has been developed by which monodisperse Fe₃O₄ NPs could be rapidly produced at a low aging temperature with high yield (90.1%). The as-synthesized NPs show excellent inductive heating and MRI properties in vitro. In contrast, Fe₃O₄ NPs synthesized by classical thermal decomposition were obtained in very low yield (20.3%) with an overall poor quality. It was found for the first time that, besides precursors and solvents, magnetic NPs themselves could be heated by microwave irradiation during the synthetic process. These findings were demonstrated by a series of microwave-heating experiments, Raman spectroscopy and vector-network analysis, indicating that the initially formed magnetic Fe₃O₄ particles were able to transform microwave energy into heat directly and, thus, contribute to the nanoparticle growth.

Introduction

Owing to their unique magnetic properties magnetite (Fe₃O₄) NPs represent an emerging class of multifunctional biomedical materials that have been used in magnetic fluid hyperthermia applications, magnetic resonance imaging (MRI), immunoassays, catalysis, and targeted drug delivery.[1–6] In spite of increasing research efforts, the controllable and stable production of uniform NPs on a commercial scale still remains a great challenge. Taking into account that the preparation of Fe₃O₄ NPs has made immense progress in the past few years, current synthetic methods are still based on conventional routes, which have been comprehensively summarized by Lu and co-workers, also listing the advantages and disadvantages of the different synthetic strategies.[7] Among them, the thermal decomposition technique enjoys a high reputation in regard to the preparation of high-quality materials, consequently many cases for the thermal decomposition synthesis of magnetic NPs with well-defined morphologies and narrow size distributions can be found in literature.[8–13] Our previous study reported the shape evolution of ferrite nanostructures with high-performance, resulting in magnetic nanomaterials that exhibit an enhanced functionality for MRI and hyperthermia.[14]

Since the reaction temperature is a key factor for the precise control of the NP monodispersity, thermal decompositions were generally performed at high temperatures around 300 °C to efficiently overcome activation energies. This assumption was well supported by a study of Hyeon et.al,[15] in which Fe₃O₄ NPs could hardly be formed when the reaction was carried out at low aging temperature of 240 °C, even when sustained for 1 day. Since the heat that was generated from a convective heating field was too low to meet the requirements of the different temperature dependences of the reaction kinetics, the vast majority of the NPs was amorphous. However, when the aging temperature was raised to 260 °C for 1 day, polydisperse NPs with poor crystallinity were finally obtained. Evidently, the inevitable problems, such as the relatively harsh reaction conditions, the high energy consumption, and the thermal gradient caused by the convective heating mode, hinder further applications of thermal decomposition methods. Therefore, a new energy-efficient and rapid approach for the sustainable production of high quality Fe₃O₄ NPs has become a particularly urgent need.

Microwave processes in general are energy and time saving, and the homogeneous heating as well as the reaction selectivity effectively reduce thermal gradient effects, thus, leading to

[a] Dr. Y.-J. Liang, Prof. Dr. Y. Zhang, Dr. T. Bai, J. Zou, Prof. Dr. N. Gu
State Key Laboratory of Bioelectronics
Jiangsu Key Laboratory for Biomaterials and Devices
School of Biological Science and Medical Engineering
Southeast University, Nanjing 210096 (P. R. China)
E-mail: zhangyu@seu.edu.cn
        guning@seu.edu.cn

[b] Prof. Dr. Y. Zhang, Prof. Dr. N. Gu
Collaborative Innovation Center of Suzhou Nano-Science and Technology
Suzhou Key Laboratory of Biomaterials and Technologies
Suzhou 215123 (P. R. China)

[c] Prof. Dr. Z. Guo
Department of Geriatrics
Second Affiliated Hospital of Nanjing Medical University
Nanjing 210029 (P. R. China)

[d] Dr. J. Xie
School of Life Science, Jiangsu Normal University
Xuzhou 221116 (P. R. China)

📖 Supporting information for this article is available on the WWW under
http://dx.doi.org/10.1002/chem.201601434.

better results.[16–19] For example, Strouse and co-workers[20] made a systematic study on how to achieve microwave-enhanced reaction rates. Later Kappe et al.[21] investigated the microwave effects on SiC (silicon carbide) vials, which could separate thermal from nonthermal effects to allow a rapid heat exchange with the reaction media. So far, studies for the rapid synthesis of Fe_3O_4 NPs have mostly employed microwave-assisted hydro- or solvothermal routes, which entirely depend on polar or ionic solvent systems.[22–24] However, there are only a few reports about microwave-assisted thermal decompositions carried out in nonpolar or weakly polar solvent systems. Hence, the further exploration of this synthetic process is particularly important, not only to study the reaction status under the microwave effect, but hopefully to circumvent the bottlenecks of thermal decomposition methods for the preparation of NPs.

Herein we present a microwave-assisted thermal decomposition procedure for the preparation of monodisperse Fe_3O_4 NPs. The classical thermal decomposition was chosen as a reference to compare and discuss the impact of the microwave irradiation on the overall quality of the synthesized Fe_3O_4 NPs. Enormous differences in terms of yield and performance between the two procedures were found under otherwise identical reaction conditions. To understand the microwave synthetic process, experiments to evaluate the heating efficiency and microwave absorptivity of the additives and as-synthesized Fe_3O_4 NPs were carried out under high(max. 850 W) or restricted microwave power (max. 200 W). The time to reach the setting reaction temperature is a key feature and a fiber-optic probe

was used for the real-time temperature tracking. The results from using two different reaction vials (i.e., a nearly microwave-transparent Pyrex vial and a highly microwave absorptive SiC vial) clearly indicated that the as-synthesized Fe_3O_4 NPs themselves (besides solvents and precursors) possess the ability to absorb microwaves. Electromagnetic measurements for the precursor and the Fe_3O_4 NPs further confirmed that as-synthesized NPs have a strong microwave dissipation at the used frequency of 2.45 GHz, which is responsible for the conversion of microwave irradiation to heat that finally leads to the ultra-fast formation of the NPs.

Results and Discussion

Structural characteristics

TEM and high-resolution TEM (HRTEM) images and selective area electron diffraction (SAED) patterns of the NPs are shown in Figure 1. TEM images demonstrate that the as-synthesized NPs by the microwave procedure are monodisperse with a spherical shape (Figure 1 A). Based on the result of HRTEM, microwave-formed NPs show a single-crystal structure and the lattice spacing of 0.216 nm and 0.254 nm could be assigned to the (400) and (311) planes of magnetite (Figure 1 B), respectively. In contrast the NPs formed by the classical thermal decomposition under identical conditions are polydisperse (Figure 1 D) with a lattice spacing of 0.294 nm for the (220) planes of magnetite (Figure 1 E). Additionally, the SAED patterns of the NPs formed by both procedures exhibit diffraction rings
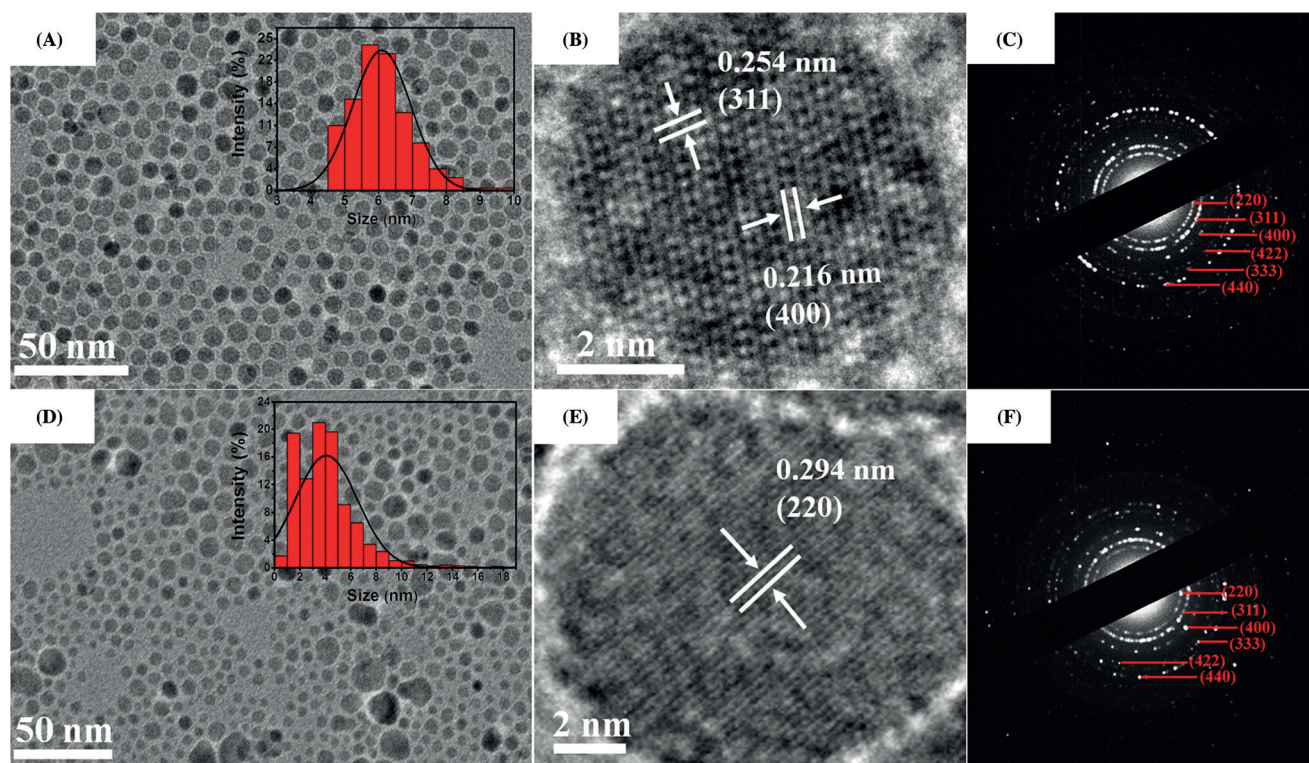
Figure 1. TEM images with corresponding size distribution histograms, high-resolution TEM (HRTEM) images, and SAED (selected area electron diffraction) patterns for Fe_3O_4 NPs obtained by A–C) microwave and D–F) thermal decomposition.

that can be attributed to the randomness of the particle orientations (Figures 1 C, F). The X-ray diffraction (XRD) patterns of the NPs (Figure S1 in the Supporting Information), which are consistent with the SAED results, further reveal that the NPs are crystalline Fe_3O_4 (JCPDS no. 89-4319).[25] However, compared with the NPs formed by thermal decomposition, the microwave-formed NPs exhibited a more intense diffraction pattern and thus possess a higher crystallinity.

Magnetic characteristics

Magnetic properties that connect very directly to biomedical applications are strongly influenced by the NP size, crystallinity, and morphology. The results from vibrating sample magnetometer (VSM) measurements show a magnetic saturation value of about 76 emu g^{-1} of the roughly 6 nm microwave-formed NPs that is higher than the values reported in the literature (Figure 2 A).[26] However, the NPs formed by thermal decomposition exhibit a severely reduced saturation magnetization of roughly 25 emu g^{-1} (Figure 2 B), which was attributed to the low crystallinity, as demonstrated above.[27–29] The insets in Fig-

ures 2 A and B depict hysteresis loops that cross the origin, indicating that almost no coercivity and remnant magnetization were observed (super-paramagnetism). In addition, in chloroform, the NPs formed by the microwave synthesis showed a typical ferrofluidic behavior when approached by a magnet. After removal of the magnet, the sample (without any aggregation of the NPs) could return to a normal state. For comparison, a solution of the NPs by thermal decomposition with an identical concentration just presented a dull response to the magnetic field.

Magnetic-induced heating measurements

The SAR (specific absorption rate) is a standard criterion that is significant for the evaluation of the magnetic-induced heating efficiency. The magnetically-induced-heating measurements in an alternating magnetic field (AMF) (390 kHz, 12 A) show an SAR of 158 W g^{-1} for the microwave-synthesized NPs, which is seven times larger than the SAR of the NPs obtained by thermal decomposition with identical reaction conditions (Figures 2 C, D). It should be noted that in previous reports, no obvi-
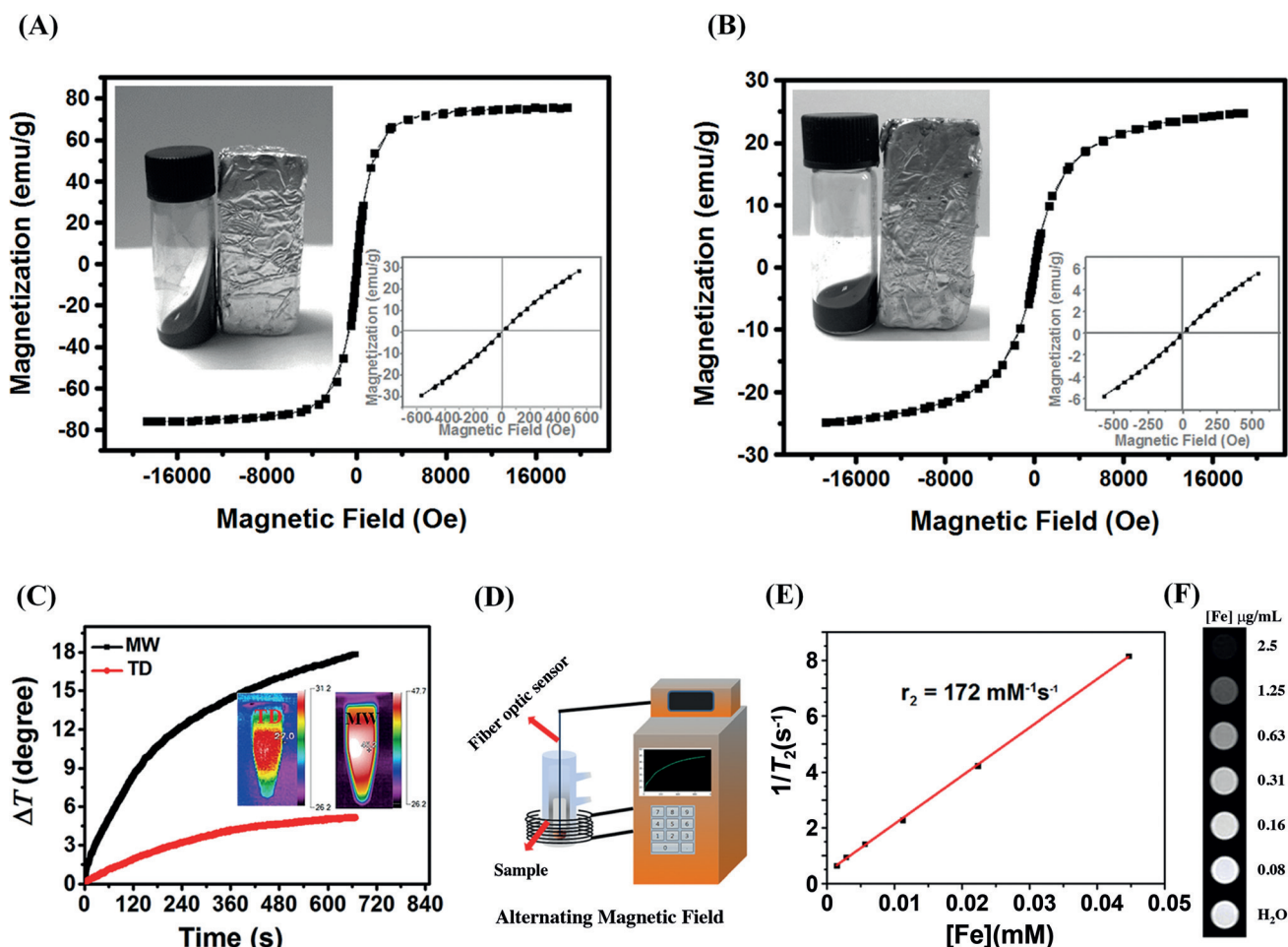
Figure 2. A) Field-dependent hysteresis loops (M–H) at room temperature for Fe_3O_4 NPs obtained by microwave synthesis (MW), and B) thermal decomposition (TD); C) Time-dependent temperature curves of Fe_3O_4 NPs for MW and TD in chloroform (2 mg [Fe]/mL) under an AMF (alternating magnetic field) at 390 kHz and 12 A (inset are near-infrared images), D) Analog experiment of magnetic induced heating; E) Plot of $1/T_2$ as a function of different Fe concentrations for microwave-formed NPs measured in a 1.5 T MR (magnetic resonance) scanner and F) T_2-weighted MR images of NPs at various Fe concentrations at 1.5 T.

ous heating behavior was observed for small NPs (ca. 6 nm), whereas our sample can elevate the temperature of chloroform (specific heat capacity of chloroform is $1.189 \, kJ \, kG^{-1} \, K^{-1}$) by more than 10 K in 3 min, which is suitable for tumor hyperthermia treatment.[30–32]

T_2-weighted MRI in vitro

The transverse relaxivity (r_2) of magnetic NPs is a standardized contrast-enhancement factor that is calculated by plotting R_2 ($R_2 = 1/T_2$) versus the molar concentration of the Fe atoms, and is positively related to the square of their magnetic moment. To our knowledge, r_2 values can be effectively tuned by the rational optimization of the NPs size, shape and even the composition,[33–34] such as the most representative T_2-weighted contrast agent WFION[35] (water-dispersible ferrimagnetic iron oxide NPs with a core size of 22 nm, $r_2 = 761 \, mM^{-1} \, s^{-1}$, which is extremely close to the theoretically predicted maximum r_2 value of ca. $800 \, mM^{-1} \, s^{-1}$), as well as Octapod-30[36] (octapod-shaped iron oxide with edge lengths of 30 nm, $r_2 = 679.25 \pm 30 \, mM^{-1} \, s^{-1}$). Consequently, the microwave-synthesized roughly 6 nm NPs possess an r_2 value of $172 \, mM^{-1} \, s^{-1}$ (Figure 2 E, F), which is higher than that of the similar sized T_2-weighted contrast agents, such as WSIO[37] (water-soluble iron oxide with a core size of 6 nm, $r_2 = 106 \, mM^{-1} \, s^{-1}$) and PIAONS[38] (polyamide stabilized iron oxide NPs with a core size of 5 nm, $r_2 = 18 \, mM^{-1} \, s^{-1}$), all due to their fine crystallinity and high magnetic moment.

Assessment of the microwave effect

We have speculated that the behavior of the microwave-formed NPs in contrast to the NPs formed by thermal decomposition under the same synthesis conditions are mainly caused by the microwave effect, which may induce heat generation that is responsible for the experimental results mentioned above. To confirm this assumption, heating experiments of different additives of the reaction system were carried out. A fiber-optic (FO) probe was utilized for the direct measurement of the local reaction temperature. The time needed to reach the highest temperature of 300 °C from room temperature (using either the maximum power of 850 W or restricted 200 W) is regarded as a key feature to evaluate the contribution of the microwave effect.

For this purpose, heating profiles were recorded in 10 mL standard microwave-transparent Pyrex and SiC vials with the same geometry and equivalent volume. First, a direct comparison of different solvents (oleic acid (OA), oleylamine (OAm) and octadecene (ODE)) either individually (4 mL), or their mixtures (OA/OAm/ODE 1 mL:2.5 mL:0.5 mL) in Pyrex vials was carried out. As shown in Figure S2 A in the Supporting Information, the reaction in the solvent mixture required the shortest time of roughly 136 s to reach 300 °C using maximum power (850 W), whereas the reaction in ODE required the longest time (ca. 377 s). The remarkable gap of the time consumption is certainly related to the vastly different microwave absorptivities of the solvents; hence, we chose the solvent mixture and

pure ODE as a fixed reference in the following tests. Accordingly, the heating profiles with 5 concentrations (0.1, 0.25, 0.4, 0.5 and 0.75 mmol) of the precursor and Fe_3O_4 NPs in ODE and mixed solvent were recorded. The time to reach 300 °C extended as the precursor concentration increased in ODE (from 382 to 429 s for 0.1–0.75 mmol, max. 850 W; Figure S2 B). The time delay in the heating profile compared to pure ODE can be ascribed to the dissipation of latent heat due to the precursor decomposition. However, the heating rate was reversed with increasing precursor concentrations in the mixed solvent (from 136 s to 104 s for 0.1–0.75 mmol, max. 850 W; Figure S2 C). Since the selective coupling in heating profiles greatly saved time, the variation to the mixed solvent system indicates that the local temperature is higher than in pure ODE, possibly caused by the evolution of nuclei or even NPs from the precursor, which would lead to a role conversion of the precursor from a thermal acceptor into a thermal supplier.

Next, Fe_3O_4 NPs were used to evaluate their microwave-absorption and thermal-transfer abilities. NP samples were prepared as mentioned in the Experimental Section by using five different precursor concentrations (0.1–0.75 mmol). The reaction time for NPs in ODE is much faster than that of pure ODE and gets further reduced with increasing NP concentrations (from 285 s to 146 s for 0.1–0.75 mmol, max. 850 W; Figure S2 B). Furthermore, addition of NPs to the mixed solvent also facilitates the reaction, leading to the shortest time to reach the setting temperature of 300 °C (from 103 s to 79 s for 0.1–0.75 mmol, max. 850 W; Figure S2 C). Therefore, NPs were confirmed to have a strong microwave-energy-conversion ability and become the major component of the thermal contribution in the described reaction process.

As an essential and helpful complement to the heating experiments, the results of the reactions obtained under restricted microwave power (max. 200 W) showed the same trend as those under maximum power (850 W), only with a higher time consumption (Figure S2 D, E, and F). As expected, heating profiles in SiC vials for solvents, precursor, and Fe_3O_4 NPs all performed with nearly identical reaction rates. Since SiC has an extremely high thermal effusivity, substances inside the vial are heated in almost the same manner (Figure S2 G, H, and I). Apparently, the result from the heating profiles in Pyrex vials clearly indicate that the heat generation and thermal transfer can be attributed to the forming NPs and the solvent mixture, which results in faster heating rates and higher reaction temperatures. In particular NPs within the microwave-transparent Pyrex vials have the potential to effectively convert the microwave energy into heat. Once the thermal saturation is reached, they would immediately act as the heat source to release and transfer the excess energy to their surroundings. Conversely, since the thermal conductivity of the SiC vial is significantly higher than that of the Pyrex vial, substances within the vial would be effectively shielded from the electromagnetic field and the heat transfer would mainly occur through the SiC walls. Note that the heating profiles with the maximum power of 850 W are prohibited for SiC vials, due to the high thermal conductivity of SiC that would lead to an exceedance of the maximum temperature limit in the microwave reactor. The

heat-transfer patterns in SiC and Pyrex vials are illustrated in Scheme S1.

Electromagnetic measurements

To further corroborate the findings mentioned above, the electromagnetic properties of the precursor and the microwave-formed Fe_3O_4 NPs were determined by a vector network analyzer (VNA). Figure S3 shows the complex permittivity (ε', ε'') and permeability (μ', μ'') between 2–18 GHz of wax composites containing a 40% mass fraction of the samples. It is known that microwave absorption properties closely correspond to the magnetic loss, dielectric loss, and impedance matching between ε'/ ε'' and μ'/μ''. Both the NPs and the precursor exhibited a stable ε' values around 5 and 3, respectively, implying that the resonance behavior of the permittivity in the microwave-frequency range should mainly originate from dipole polarization and interfacial polarization. Similar circumstances are also observed in the ε'' curve, except that the resonant peaks are weaker with maximum values of 0.02 and −0.03 at 3 GHz, respectively. Furthermore, several small peaks, which are up to sixfold increased compared to the precursor spectrum, can be seen in the NP frequency-dependence spectrum up to 14 GHz. In addition, both the real (μ') and imaginary parts (μ'') of the NP sample exhibited a relaxation behavior with significantly decreasing values compared to the precursor of 1.2 to 0.8 and 0.75 to 0.05 at frequencies of 5 and 7 GHz, respectively. It is worth mentioning that the magnetic energy is transferred into electric energy since the ε'' value of the NPs is enhanced, which leads to a μ'' value declining sharply into nearly zero; however, a resonance behavior with a steady decline can be ignored for precursors based on the Maxwell equations.[39]

Microwave magnetic loss of magnetic materials mainly originates from the eddy current effect, hysteresis, and magnetic resonance (composed of domain wall and natural ferromagnetic resonance). Considering that the magnetic loss tangent $\tan \delta_\mu$[17,40–41] of small NPs declines sharply with rising frequency to reach its steepest value of 0.53 at 2.4 GHz and continually decreases afterwards up to 7 GHz, the contribution of the domain-wall resonance may be neglected (Figure S3 E). On the other hand, the values of $\mu''(\mu')^{-2}f^{-1}$ should be constant along with the frequency enhancement if the magnetic loss is only derived from the eddy current loss. Herein, sample values for $\mu''(\mu')^{-2}f^{-1}$ only change by about 0.007 between 8–18 GHz, hence, the eddy current loss greatly contributes to μ'' and the magnetic loss in this frequency range (Figure S3 F). These features suggest that the high μ'' value and the large magnetic loss were achieved all owing to defects of the small NPs based on a rotation mechanism, which could hinder the spin rotation that would predominantly contribute to the permeability in the 2–18 GHz range.[42–43] Moreover, the refection loss (RL) reached −15 dB for the NP composite at 3 GHz and 10 mm thickness (Figure 3 A). However, the precursor at the same coating thickness only achieves a maximum RL value of −2.8 dB at 13 GHz, hence, the precursor hardly absorbs microwaves (Figure 3 B). Additionally, the projection of the RL for the NP samples in the basal plane is increased with decreasing fre-
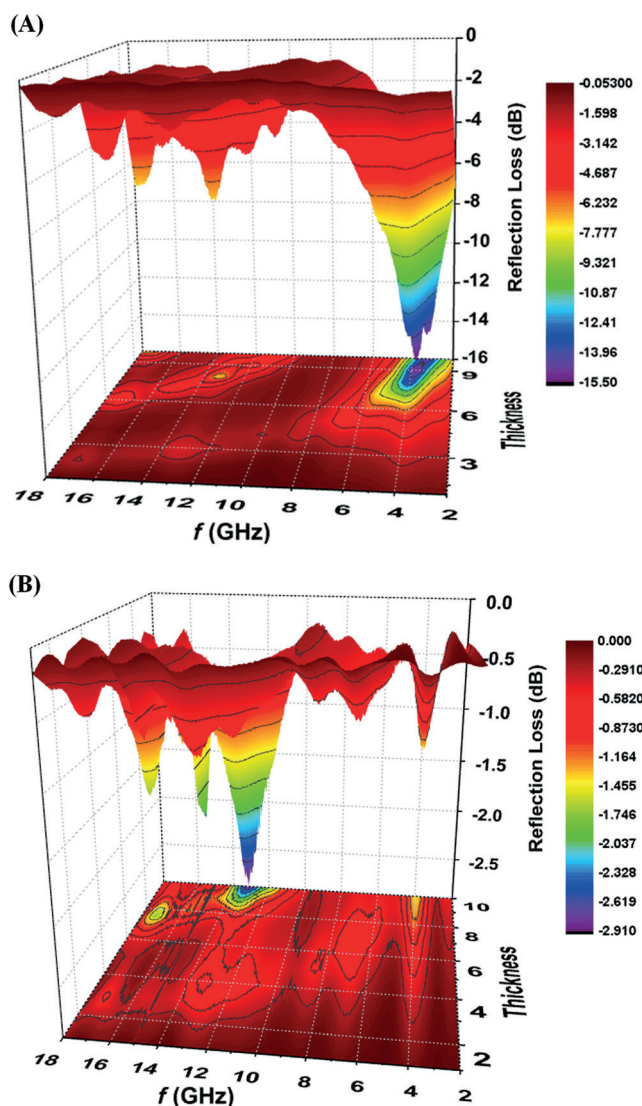

Figure 3. Frequency and thickness dependence of the reflection loss (RL) for A) microwave-formed Fe_3O_4 NPs, and B) precursor with the wax composite in different thicknesses.

quency at a given permittivity and permeability. Notably, a considerable RL for bandwidths less than −10 dB covers a range of 2–4 GHz with the maximal reflectivity loss located in the S-band, which strongly demonstrates the conversion of electromagnetic energy, and also confirms that our NPs are promising microwave absorbing materials in 2.45 GHz microwave reactors.

Understanding the microwave synthetic process

The results based on the accurate heating profiles and microwave electromagnetic measurements are helpful for understanding the synthetic process from a new perspective. In a microwave approach, the curve of the reaction process (Scheme 1 A) presents the rapid heat generation in the first step derived from the interaction between the mixed solvent and the microwave irradiation. The pressure in the airtight reaction container starts rising when the reaction temperature
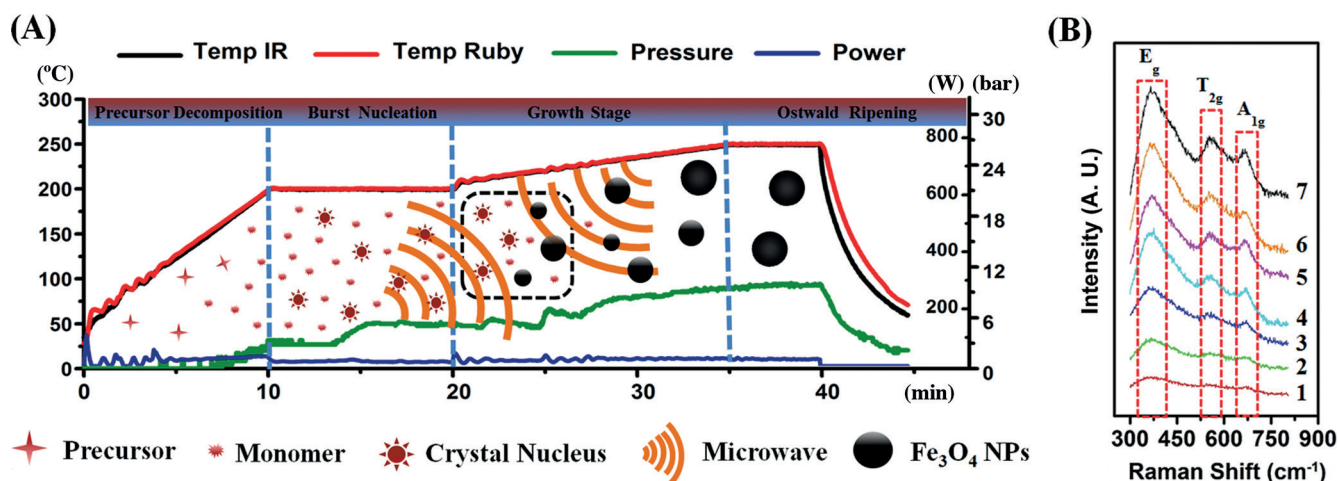
Scheme 1. A) Schematic presentation of the synthetic mechanism and real-time recording of the microwave synthesis of the Fe_3O_4 NPs. The data include temperature, pressure, and power monitored by a Monowave 300 (IR infrared detector, Ruby fiber-optic probe). B) Raman samples 1–7(S1–S7) were taken out from reaction mixture at: 1) 180 °C; 2) 200 °C, 0 min; 3) 200 °C, 10 min; 4) 220 °C; 5) 235 °C; 6) 250 °C, 0 min, and 7) 235 °C, 5 min.

reaches roughly 157 °C and rises quickly up to 200 °C, at which the precursor was completely dissolved and burst nucleation proceeded. In succession, small and temporarily unstable nanocrystals were obtained along with the gradually increasing pressure. Remarkably, these small crystals served as disorder magnets and absorb microwaves for the electromagnetic energy transformation. The low stability nanocrystals with large surface-to-volume ratios keep growing to produce more stable and larger crystals that continually reinforce the thermal generation at a stable rate, until the mixture was further heated to 250 °C. The heat keeps the Ostwald ripening progress running smoothly after staying at 250 °C for 5 min. Microwave irradiation favors a dramatic enhancement of the burst nucleation and the homogeneous growth process, in which the sufficient reaction heat and adequate pressure are regarded as a coordinated action that could effectively narrow down the gap between nucleation and growth process to fabricate good quality nanocrystals with high yield.

Raman spectroscopy provides key evidence to identify the features of chemical bonding, the degrees of crystallization, and matter–phase transitions. Five active Raman modes ($A_{1g} + E_g + 3T_{2g}$) exist in the range of 200–800 cm^{-1} for Fe_3O_4, which were assigned to the different forms of oxygen and iron ions.[44–46] To further confirm the assumption of the rapid nucleation process in the microwave synthesis mentioned above, we took samples from the reaction at certain time intervals and analyzed their Raman signals. Scheme 1B shows the Raman spectra of the NPs in the temperature range from 180 to 250 °C. The typical Raman vibration modes of the samples can be assigned as E_g (362–366 cm^{-1}), symmetrical T_{2g}(550–556 cm^{-1}), and A_{1g} (665–670 cm^{-1}). While performed in the initial crystallization stage (ca. 180–200 °C, Scheme 1, 1 and 2), the Raman signal is too broad to be clearly identified, but it is related to oxygen defects or finite size effects.[47] In later stages, an anomalous peak broadening was observed in the nucleation and growth phase (Scheme 1, 3 and 4), owing to mostly cation-related and structural oxygen defects. Once the

defects occupy the crystal surface to induce lattice distortion, the corresponding geometrical phonon scattering would be affected by structural fluctuations that lead to phonon-vibration-frequency changes.[48] In the following growth and aging stage (ca. 220–250 °C), the Raman peaks are becoming sharper (Scheme 1, 5–7), which account for the gradual and uniform increase in crystallinity and size, resulting in less defects in the NPs.

Turning to the thermal decomposition process, the concentration of the monomers has been schematically plotted as a function of time. The reaction undergoes the nucleation process at 220–240 °C, following the LaMer nucleation theory, triggered by the dissociation of $Fe(acac)_3$, until the concentration of the precursor decreases to a critical threshold and the dissociation stops. Similarly, the Ostwald ripening takes place accompanied by time and thermal consumption. Since the convective-heating pattern mostly depends on parameters such as specific heat capacity, viscosity, and heat-transfer coefficient, the nucleation and growth stage cannot be completely separated here, due to the applied insufficient temperature and reaction-time range. In particular, the production of high-quality NPs in this way is only possible when the temperature dependence of the nucleation and growth kinetics is rigorously taken into account, which explains why the inhomogeneity of the nucleation and growth process can be traced to the inefficient transfer of thermal energy from the convective heating.[20,49–51]

Conclusion

In summary, we have developed a practical procedure that combines the advantages of both thermal decomposition and the microwave technique, for the fabrication of high-quality Fe_3O_4 NPs. The synthetic strategy makes use of microwave-selective heating without suffering harsh conditions, unlike thermal decomposition based on black-body radiation heat. The investigation of the ultrafast formation of the Fe_3O_4 NPs shows

that magnetic NPs are able to effectively convert microwave energy even at higher rates than other additives and are responsible for the observed reaction-rate enhancement, although the aging period proceeded at 250 °C for only 5 min. In our opinion, the thermal contribution of the Fe_3O_4 NPs has been neglected too often, because the high selectivity of the heating coupled by polar solvents was always recognized as the dominant heat source. Consequently, our study not only looks at commonly known microwave procedures from a fresh perspective, but could also be applied to fabricate other functional nanomaterials in a highly efficient way.

Experimental Section

Microwave-assisted thermal decomposition synthesis of Fe_3O_4 NPs

The single-mode microwave system (Monowave 300) used for synthesizing the Fe_3O_4 NPs was made by Anton-Paar (Austria). The system operates at a frequency of 2.45 GHz with a maximum power of 850 W. Pressure and temperature could be simultaneously monitored by an external infrared sensor (IR) and an internal fiber-optic (FO) probe. Only SiC and Pyrex vials suitable for this microwave system have been used to prevent accidents during reactions at the maximum values of 300 °C and 30 bar.

Our synthetic strategy is schematically illustrated in Scheme S2 in the Supporting Information. The ideal Fe_3O_4 NPs (ca. 6 nm in size) were obtained by the following microwave procedure: Ferric acetylacetonate [Fe(acac)$_3$] (1 mmol) was added to the mixed solvent at the proper ratio (4 mL OA, 10 mL OAm, and 2 mL ODE) in a 30 mL Pyrex vial, operated with the Monowave 300 under maximum microwave power (850 W). The mixture was heated to 200 °C from room temperature in 10 min and kept there for 10 min. Afterwards, the temperature was further increased to 250 °C in 15 min then kept stable for 5 min until the reaction was completed. Subsequently, the system was cooled down to 60 °C by compressed air in approximately 3 min. After the five operation steps, the NPs were washed with ethanol and acetone and dried in a vacuum oven to give a final product yield of 69.7 mg (90.1 %).

Thermal decomposition synthesis of Fe_3O_4 NPs

To compare the thermal decomposition to the microwave synthesis, the reaction was performed with an equivalent procedure (without microwave irradiation), except sufficient stirring under a flow of N_2 and "natural" cooling to 60 °C for about 35 min. The as-synthesized NPs were also handled in the same way to give a calculated yield of only 15.7 mg (20.3 %).

Characterization of the Fe_3O_4 NPs

The morphology of the as-synthesized Fe_3O_4 NPs was analyzed by transmission electron microscopy (TEM), high-resolution TEM (HRTEM), and selected area electron diffraction (SAED) using a Tokyo JEOL JEM-2100. Powder X-ray diffraction (XRD) spectra were recorded on a Bruker X-ray diffractometer (D8-Discover) operated at 40 mA and 40 kV. Magnetic properties of the NPs obtained by thermal decomposition and microwave irradiation were investigated in a vibrating sample magnetometer (VSM, Lakeshore 7407) at room temperature. Iron concentrations of the NPs were evaluated by the classical 1,10-phenanthroline (phen) complexation method based on the C–A (absorbance versus iron concentration)

calibration curve observed by UV/Vis spectrophotometry (Shimadzu, UV-3600). Simulation of the magnetic inductive heating was accomplished in alternating magnetic fields (Shuangping SPG-06-II, China, under 390 kHz, 12 A). Phantom experiments in vitro were carried out on a clinical 1.5 T MR scanner (Siemens, Avanto). The electromagnetic performance was measured by a vector network analyzer (Agilent N5224 A). Samples were pressed into a toroidal shape of 7.00 mm outer diameter and 3.04 mm inner diameter under the frequency range of 2–18 GHz. Raman measurements were performed with an inVia Raman microscope (Renishow, UK) utilizing a 785 nm Argonion laser as excitation source (sample in quartz slides, 1 mW power with 3-times 30 s acquisition time).

Magnetic-induced-heating measurements

Measurement of the heat generation of the Fe_3O_4 NPs in vitro was accomplished using a magnetic-heating system (Shuangping SPG-06-II, China) that produces an alternating magnetic field (AMF). Samples obtained from the microwave and thermal decomposition synthesis at uniform concentrations were placed inside a copper coil under an AMF. The temperature was measured with a FOT-L-BA fiber optic temperature sensor (FISO, Canada). The specific absorption rate (SAR) is defined as the power absorbed (which is converted to heat) per mass of magnetic material (W g^{-1}) and is strongly connected to the AMF system variables, such as the field frequency and amplitude, the inductive coil dimensions, the solvent carrier, and the shape and size of the nanostructures. The temperature rise was determined by this process from the mean slope of the $\Delta T/\Delta t$ function. Then the SAR values were calculated by means of Equation (1)[52], in which C is the specific heat capacity of the different species in solution, $\Delta T/\Delta t$ stands for the initial slope of the temperature versus time curve, m_i is the weight of the whole suspension, and m_n the total mass of the magnetic material in the suspension.

$$SAR = C \frac{\Delta T}{\Delta t} \frac{m_i}{m_n} \tag{1}$$

The SAR value is a standard criterion for the quantification of the heating efficiency of superparamagnetic NPs and is highly dependent on theoretical models supported by the magnetic relaxation (Brownian relaxation and Neel relaxation). Magnetic hyperthermia (MH) is a promising method for the treatment of cancer.

T_2-weighted MRI

The T_2-weighted MR images were determined by a multi-echo spin-echo sequence (16 echoes; repetition time 2500 ms; echo time 22–352 ms). The T_2 relaxation times for six different samples (Fe concentrations of 0.078, 0.156, 0.3125, 0.625, 1.25, and 2.5 µg mL^{-1}) were obtained by calculating the signal intensities in a 0.3 cm^2 region.

Electromagnetic measurements

Magnetic- and dielectric-signature measurements were carried out using a vector network analyzer (Agilent N5224 A). The as-prepared NPs and the precursor were ground to powders and homogenously dispersed with wax at a mass ratio of 3:2. The permeability and permittivity of the samples was measured by a coaxial transmission–reflection method with a sample thickness between 1–10 mm in a frequency range of 2–18 GHz. Notably, a full two-port calibration was initially performed to remove errors. Based on the transmission-line theory, the reflection loss (RL) value for a single-layer

absorber on a metal plate can be calculated from the measured electromagnetic parameters, which are consistent with the permeability and permittivity at a given frequency and coating thickness following Equations (2) and (3)[53], in which f is the matching frequency, d is the thickness of the sample, c is the speed of light, Z_0 is the impedance of air, and Z_{in} is the input impedance of the sample.

$$Z_{in} = Z_0 \sqrt{\frac{\mu_r}{\varepsilon_r}} \tanh\left(j \frac{2\pi fd}{c} \sqrt{\mu_r e_r} \right) \tag{2}$$

$$RL = 20 \log_{10} \left| \frac{z_0 - z_{in}}{z_0 + z_{in}} \right| \tag{3}$$

Importantly, the RL of dual-loss samples was carried out to further investigate the influence of the magnetic and the dielectric loss, respectively. In particular, the RL curves are dominated by the contribution of the electromagnetic-wave interference with the interface and by the microwave absorption, and could reach minimum values when the sample coating thickness (d_m) and frequency (f_m) satisfy the quarter-wavelength-matching ($\lambda/4$) relationship [Eq. (4)].[54-55]

$$d_m = \frac{n\,c}{4 f_m \sqrt{\mu_r e_r}} \tag{4}$$

Acknowledgements

[1] D. L. Leslie-Pelecky, R. D. Rieke, *Chem. Mater.* **1996**, *8*, 1770–1783.
[2] S. Laurent, D. Forge, M. Port, A. Roch, C. Robic, L. Vander Elst, R. N. Muller, *Chem. Rev.* **2008**, *108*, 2064–2110.
[3] C. S. Kumar, F. Mohammad, *Adv. Drug Delivery Rev.* **2011**, *63*, 789–808.
[4] L. Z. Gao, J. Zhuang, L. Nie, J. B. Zhang, Y. Zhang, N. Gu, T. H. Wang, J. Feng, D. L. Yang, S. Perrett, X. Y. Yan, *Nat. Nanotechnol.* **2007**, *2*, 577–583.
[5] N. Lee, T. Hyeon, *Chem. Soc. Rev.* **2012**, *41*, 2575–2589.
[6] D. Ling, T. Hyeon, *Small* **2013**, *9*, 1450–1466.
[7] A. H. Lu, E. L. Salabas, F. Schüth, *Angew. Chem. Int. Ed.* **2007**, *46*, 1222–1244; *Angew. Chem.* **2007**, *119*, 1242–1266.
[8] T. Hyeon, S. S. Lee, J. Park, Y. Chung, H. B. Na, *J. Am. Chem. Soc.* **2001**, *123*, 12798–12801.
[9] S. H. Sun, H. Zeng, *J. Am. Chem. Soc.* **2002**, *124*, 8204–8205.
[10] S. H. Sun, H. Zeng, D. B. Robinson, S. Raoux, P. M. Rice, S. X. Wang, G. X. Li, *J. Am. Chem. Soc.* **2004**, *126*, 273–279.
[11] S. Peng, S. H. Sun, *Angew. Chem. Int. Ed.* **2007**, *46*, 3865–3869; *Angew. Chem.* **2007**, *119*, 3939–3943.
[12] W. W. Yu, J. C. Falkner, C. T. Yavuz, V. L. Colvin, *Chem. Commun.* **2004**, *20*, 2306–2307.
[13] Z. J. Zhou, X. L. Zhu, D. J. Wu, Q. L. Chen, D. T. Huang, C. J. Sun, J. Y. Xin, K. Y. Ni, J. H. Gao, *Chem. Mater.* **2015**, *27*, 3505–3515.
[14] J. Xie, C. Z. Yan, Y. Zhang, N. Gu, *Chem. Mater.* **2013**, *25*, 3702–3709.
[15] J. Park, K. An, Y. Hwang, J. G. Park, H. J. Noh, J. Y. Kim, J. H. Park, N. M. Hwang, T. Hyeon, *Nat. Mater.* **2004**, *3*, 891–895.
[16] M. Baghbanzadeh, L. Carbone, P. D. Cozzoli, C. O. Kappe, *Angew. Chem. Int. Ed.* **2011**, *50*, 11312–11359; *Angew. Chem.* **2011**, *123*, 11510–11561.
[17] Y. J. Zhu, F. Chen, *Chem. Rev.* **2014**, *114*, 6462–6555.
[18] M. B. Gawande, S. N. Shelke, R. Zboril, R. S. Varma, *Acc. Chem. Res.* **2014**, *47*, 1338–1348.
[19] H. J. Kitchen, S. R. Vallance, J. L. Kennedy, N. Tapia-Ruiz, L. Carassiti, A. Harrison, A. Gavin Whittaker, T. D. Drysdale, S. W. Kingman, D. H. Gregory, *Chem. Rev.* **2014**, *114*, 1170–1206.
[20] J. A. Gerbec, D. Magana, A. Washington, G. F. Strouse, *J. Am. Chem. Soc.* **2005**, *127*, 15791–15800.
[21] D. Obermayer, B. Gutmann, C. O. Kappe, *Angew. Chem. Int. Ed.* **2009**, *48*, 8321–8324; *Angew. Chem.* **2009**, *121*, 8471–8474.
[22] B. Babita, M. N. Nadagouda, R. S. Varma, *J. Phys. Chem. C* **2008**, *112*, 18399–18404.
[23] H. Y. Hu, H. Yang, P. Huang, D. X. Cui, Y. Q. Peng, J. C. Zhang, F. Y. Lu, J. Lian, D. L. Shi, *Chem. Commun.* **2010**, *46*, 3866–3868.
[24] O. Pascu, E. Carenza, Martí. Gich, S. Estradé, F. Peiró, G. Herranz, A. Roig, *J. Phys. Chem. C* **2012**, *116*, 15108–15116.
[25] N. N. Song, H. T. Yang, H. L. Liu, X. Ren, H. F. Ding, X. Q. Zhang, Z. H. Cheng, *Sci. Rep.* **2013**, *3*, 3161.
[26] N. Z. Bao, L. M. Shen, Y. Wang, P. Padhan, A. Gupta, *J. Am. Chem. Soc.* **2007**, *129*, 12374–12375.
[27] T. Kim, M. Shima, *J. Appl. Phys.* **2007**, *101*, 09M516.
[28] J. M. D. Coey, *Phys. Rev. Lett.* **1971**, *27*, 1140–1141.
[29] M. P. Morales, S. Veintemillas-Verdaguer, M. I. Montero, C. J. Serna, A. Roig, L. Casas, B. Martínez, F. Sandiumenge, *Chem. Mater.* **1999**, *11*, 3058–3064.
[30] J. P. Fortin, C. Wilhelm, J. Servais, C. Ménager, J. C. Bacri, F. Gazeau, *J. Am. Chem. Soc.* **2007**, *129*, 2628–2635.
[31] S. Laurenta, S. Dutz, U. O. Häfelib, M. Mahmoudi, *Adv. Colloid Interface Sci.* **2011**, *166*, 8–23.
[32] F. Sonvico, S. Mornet, S. Vasseur, C. Dubernet, D. Jaillard, J. Degrouard, J. Hoebeke, E. Duguet, P. Colombo, P. Couvreur, *Bioconjugate Chem.* **2005**, *16*, 1181–1188.
[33] N. Lee, D. Yoo, D. H. Ling, M. H. Cho, T. Hyeon, J. Cheon, *Chem. Rev.* **2015**, *115*, 10637–10689.
[34] J. Mohapatra, A. Mitra, H. Tyagi, D. Bahadur, M. Aslam, *Nanoscale* **2015**, *7*, 9174–9184.
[35] N. Lee, Y. Choi, Y. Lee, M. Park, W. K. Moon, S. H. Choi, T. Hyeon, *Nano Lett.* **2012**, *12*, 3127–3131.
[36] Z. Zhao, Z. Zhou, J. Bao, Z. Wang, J. Hu, X. Chi, K. Ni, R. Wang, X. Chen, Z. Chen, J. Gao, *Nat. Commun.* **2013**, *4*, 2266.
[37] Y. W. Jun, Y. M. Huh, J. S. Choi, J. H. Lee, H. T. Song, S. Kim, S. Yoon, K. S. Kim, J. S. Shin, J. S. Suh, J. Cheon, *J. Am. Chem. Soc.* **2005**, *127*, 5732–5733.
[38] R. Hao, J. Yu, Z. G. Ge, L. Y. Zhao, F. G. Sheng, L. L. Xu, G. J. Li, Y. L. Hou, *Nanoscale* **2013**, *5*, 11954–11963.
[39] N. A. Buznikov, *J. Phys. D* **2010**, *43*, 055002.
[40] C. O. Kappe, *Chem. Soc. Rev.* **2008**, *37*, 1127–1139.
[41] C. Gabriel, S. Gabriel, E. H. Grant, B. S. Halstead, D. M. P. Mingos, *Chem. Soc. Rev.* **1998**, *27*, 213–223.
[42] N.-N. Song, Y.-J. Ke, H.-T. Yang, H. Zhang, X.-Q. Zhang, B.-G. Shen, Z.-H. Cheng, *Sci. Rep.* **2013**, *3*, 2291.
[43] Z. Z. Wang, H. Bi, P. H. Wang, M. Wang, Z. W. Liu, L. Shen, X. S. Liu, *Phys. Chem. Chem. Phys.* **2015**, *17*, 3796–3801.
[44] I. Chourpa, L. Douziech-Eyrolles, L. Ngaboni-Okassa, J. F. Fouquenet, S. Cohen-Jonathan, M. Souce, H. Marchais, P. Dubois, *Analyst* **2005**, *130*, 1395–1403.
[45] D. L. A. de Faria, S. Venancio Silva, M. T. de Oliveira, *J. Raman Spectrosc.* **1997**, *28*, 873–878.

[46] O. N. Shebanova, P. Lazor, *J. Raman Spectrosc.* **2003**, *34*, 845 – 852.

[47] A. Rečnik, I. Nyirő-Kósa, I. Dódony, M. Pósfai, *CrystEngComm* **2013**, *15*, 7539 – 7547.

[48] Z. Cvejic, S. Rakic, A. Kremenovic, B. Antic, C. Jovalekic, P. Colomban, *Solid State Sci.* **2006**, *8*, 908 – 915.

[49] N. T. K. Thanh, N. Maclean, S. Mahiddine, *Chem. Rev.* **2014**, *114*, 7610 – 7630.

[50] V. K. LaMer, R. H. Dinegar, *J. Am. Chem. Soc.* **1950**, *72*, 4847 – 4854.

[51] C. Yang, J. J. Wu, Y. L. Hou, *Chem. Commun.* **2011**, *47*, 5130 – 5141.

[52] B. Mehdaoui, A. Meffre, J. Carrey, S. Lachaize, L. M. Lacroix, M. Gougeon, B. Chaudret, M. Respaud, *Adv. Funct. Mater.* **2011**, *21*, 4573 – 4581.

[53] A. N. Yusoff, M. H. Abdullah, S. H. Ahmad, S. F. Jusoh, A. A. Mansor, S. A. A. Hamid, *J. Appl. Phys.* **2002**, *92*, 876 – 882.

[54] T. Inui, K. Konishi, K. Oda, *IEEE. Trans. Magn.* **1999**, *35*, 3148 – 3150.

[55] B. C. Wang, J. Q. Wei, Y. Yang, T. Wang, F. S. Li, *J. Magn. Magn. Mater.* **2011**, *323*, 1101 – 1103.